Open access • Proceedings Article • DOI:10.1109/ICPE.2015.7168088

Analysis of coupled-inductor configuration for an interleaved high step-up converter

Wilmar Martinez, Jun Imaoka, Yuki Itoh, Masayoshi Yamamoto ...+1 more authors

Institutions: Shimane University, Okayama University

Published on: 01 Jun 2015 - International Conference on Performance Engineering

Topics: Boost converter, Buck–boost converter, Ćuk converter, Buck converter and Forward converter

Analysis of Coupled-Inductor Configuration for an Interleaved High Step-Up Converter

Wilmar Martinez[1], Jun Imaoka[1], Yuki Itoh[1], Masayoshi Yamamoto[1] and Kazuhiro Umetani[2]
[1] Shimane University, Japan
[2] Okayama University, Japan

***Abstract*-- High step-up converters are widely used in sustainable energy systems and recently used in automotive applications due to their high voltage gain capability. Nevertheless, with the purpose of obtaining a higher voltage gain, in comparison with conventional boost converters, current high step-up converters often employ additional multiplier cells, which may lead to significant cost-up and low power density. Therefore, a novel two-phase interleaved high step-up converter is proposed in order to minimize additional circuit volume used to achieve large voltage gain. The proposed converter addresses the purpose by a particular coupled inductor where three windings are installed in one or two cores. As a result, the proposed converter can achieve higher voltage gain than the conventional topologies by adding a winding and two diodes to the interleaved two phase boost chopper, besides the coupled-inductor configuration. This paper evaluates two arrangements of the coupled-inductor configuration of the proposed high step-up converter: 1. Three windings integrated in only one core and 2. Two independent inductors with a shared winding. The result revealed that the proposed converter shows higher voltage gain than the normal boost converter and the magnetic integration in the coupled-inductor configuration further increases the voltage gain by 20%.**

***Index Terms*-- Coupled-Inductor, High Step-Up Converter, Hybrid Electric Vehicles, Power Density.**

I. INTRODUCTION

High step-up converters are recognized as useful circuits for many applications where the low voltage of the power supply needs to be boosted in order to obtain the higher voltage required by the load [1]-[5]. In these applications, conventional boost topologies usually present drawbacks due to two main reasons: 1. A high duty ratio is needed to obtain the required output voltage which produces extremely high losses in the semiconductors due to the parasitic effects, and 2. Conventional boost converters cannot achieve a high voltage gain because the parasitic resistances and parasitic inductances produced large voltage drops [6]-[10].

Consequently, the demand of high step-up conversion techniques has gradually increased according to the downsizing requirements and low-voltage energy sources in Electric Vehicle (EV) applications [11]-[15].

In response to this demand, several high step-up topologies have been proposed with the use of autotransformers or multiplier cells. In these converters, additional capacitors, inductors or semiconductors are used in order to store energy and obtain a high voltage gain [16]–[20]. However, these additional components increase the circuit volume; and in some cases, it may lead to significant cost-up.

This study addresses the problem by proposing a novel high step-up converter with a few additional components. Our strategy is focused on combining the following two techniques: 1. The interleaved two-phase boost chopper topology, 2. The integrated magnetics. The interleaved two-phase technique is known as effective to reduce the volume of the output capacitor. Moreover, this technique might produce a reduction of the inductor volume because it allows smaller inductance for the input inductors to suppress the input current ripple. On the other hand, integrated magnetics is a well-known technique reported as effective to increase the power density and miniaturize magnetic components [21]-[24]. These techniques are used in order to obtain a novel and improved high step-up power converter with high power density. Fig. 1 shows the schematic of the proposed high step-up converter.

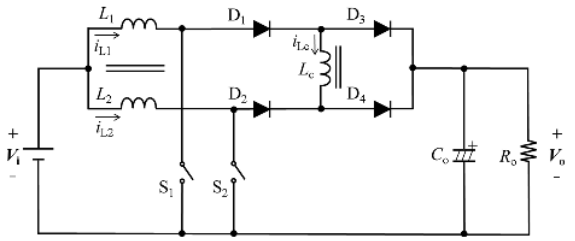

Fig. 1. Proposed high step-up converter.

This converter can be constructed with two different core configurations: The first one is the two-core coupled inductor version, which is composed of an additional winding L_C wound on normal inductors for L_1 and L_2. The second one is the integrated coupled-inductor version, which magnetically integrates the two-core coupled inductor into only one core.

In this study, the performance evaluation of the two coupled-inductor configurations of the proposed converter is presented. This evaluation is conducted with the purpose of establishing the suitable core configuration which offers the highest voltage gain.

This paper is organized as follows: First, the review of the operation principle of the proposed converter is

presented. Second, each coupled-inductor configuration is introduced and the voltage gain of the proposed converter is presented. Then, the magnetic modeling of each coupled-inductor configuration is presented. Finally, experimental test results of three 100W prototypes are shown as a validation of the proposed converter and as an experimental comparison of the two coupled-inductor configurations and the conventional interleaved boost converter.

II. Review of the Proposed Converter

A. Circuit Configuration

The proposed high step-up converter, shown in Fig. 1, is a two-phase interleaved boost converter composed of a particular magnetic coupled-inductor composed by three windings that can be installed in different core configurations. There are two winding, L_1 and L_2, connected to the power source and a third winding L_c, defined as central winding, located between the cathodes of D_1 and D_2. For convenience, we define the positive terminal of L_c as the node where the cathode of D_1 and the anode of D_3 are connected.

In addition, this converter has two power switches S_1 and S_2 which are alternative commuted with a 180 degree phase difference between them, four diodes D_1-D_4 and one output capacitor C_o.

B. Coupled-Inductor Configurations

As it was mentioned above, the proposed converter has a novel coupled-inductor that downsize the magnetic components and increase the voltage gain.

In this context, two configurations of coupled inductor that achieve these features are proposed: The first one is the Integrated Coupled-Inductor (ICI), where the three windings are installed into only one EE core, in which, L_1 and L_2 are wound in the external legs of the EE core and L_c is wound in the central leg, as shown in Fig. 2.

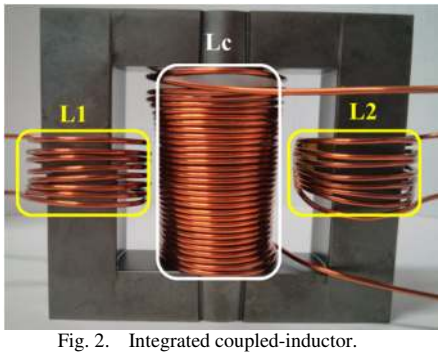

Fig. 2. Integrated coupled-inductor.

Moreover, the external windings are directly coupled and an air-gap is installed in each external leg in order to suppress excessive DC flux induction.

On the other hand, the second configuration is the Two Cores Coupled-Inductor (TCCI), where two EE cores are used in order to integrate the windings. As Fig. 3 shows, L_1 and L_2 are independently wound in the central leg of each EE core. Each of these windings is wound in different direction with the purpose of emulating the direct coupling of the ICI configuration. In addition, L_c is wound around the windings L_1, L_2 and the central legs of both EE cores, see Fig. 3. The purpose of this approach is to obtain a magnetic coupling between the windings L_1, L_2 and L_c.

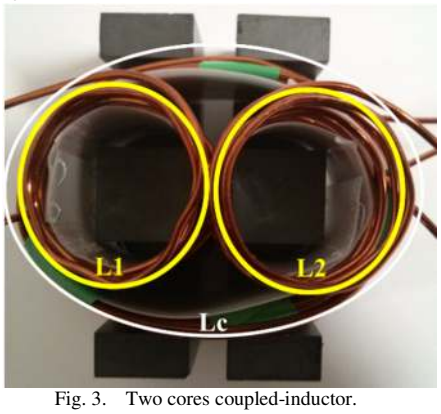

Fig. 3. Two cores coupled-inductor.

In both configurations, there are two independent magnetic fluxes ϕ_1 and ϕ_2, and one shared flux ϕ_c as shown in Fig. 4 and Fig. 5.

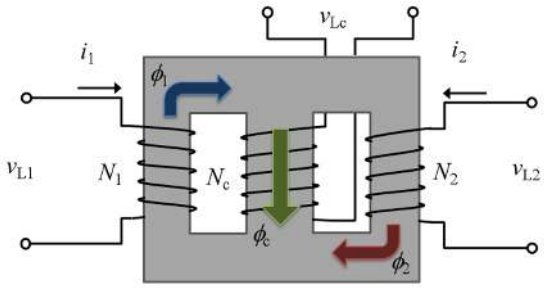

Fig. 4. Magnetic flux in the integrated coupled-inductor.

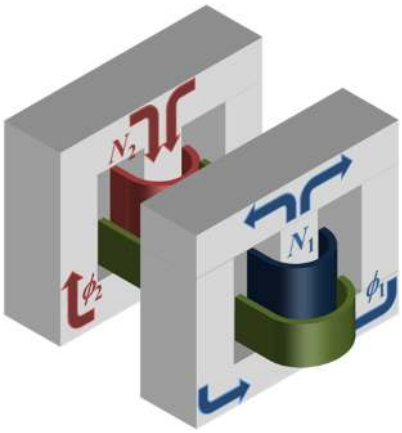

Fig. 5. Magnetic flux in the two cores coupled-inductor.

C. Induced Voltage in Each Winding

With the purpose of deriving the voltage gain expression of the proposed converter, the induced voltage in each winding is required. Therefore, the induced voltage in each of the three windings is defined as follows:

$$\begin{cases} v_{L1} = N_1 \dfrac{d\phi_1}{dt} \\ v_{L2} = N_2 \dfrac{d\phi_2}{dt} \\ v_{LC} = N_C \dfrac{d\phi_C}{dt} \end{cases} \quad (1)$$

Where, v_{L1}, v_{L2} and v_{LC} are the winding voltages; N_1, N_2 and N_c are the number of turns of each winding L_1, L_2 and L_c, respectively; and ϕ_1, ϕ_2 and ϕ_c are the magnetic fluxes interlinking with the windings L_1, L_2 and L_c, respectively. Moreover, for the symmetry between the two phases, we assume N_a=N_1=N_2. Additionally, according to Fig. 4 and Fig. 5, we have:

$$\phi_C = \phi_1 - \phi_2 \quad (2)$$

Therefore, the induced voltage in the central winding, of each core configuration, is produced by the applied voltage to the windings L_1 and L_2 as follows:

$$v_{LC} = \frac{N_c (v_{L1} - v_{L2})}{N_a} \quad (3)$$

For convenience, we introduce N as the ratio of the number of turns of the central winding and the number of turns of L_1 or L_2.

$$N = \frac{N_c}{N_a} \quad (4)$$

Finally, substituting (4) into (3), we can find the induced voltage in the central winding in function of the voltage of L_1 and L_2.

$$v_{LC} = N(v_{L1} - v_{L2}) \quad (5)$$

III. Steady State Analysis

A. Operating Modes

The two-phase interleaved high step-up converter presents four different operation modes corresponding to all the combinations of the ON and OFF-state of the switches, as shown in Fig. 6. In addition, Fig. 6 shows the operating waveforms of the proposed converter when it is under an ideal operation when the duty cycle d is lower and higher than 50%.

In this context, Fig. 7 shows the overall operation modes of the proposed converter.

Mode 1: As Fig. 6 and Fig. 7(a) show, S_1 is turned ON and S_2 is turned OFF, where i_1 flows only through the external winding L_1. On the other hand, i_2 flows through L_2, D_2, D_3, L_C and C_o. Moreover, a negative voltage is induced in the central winding as a result of the voltage applied to the external windings.

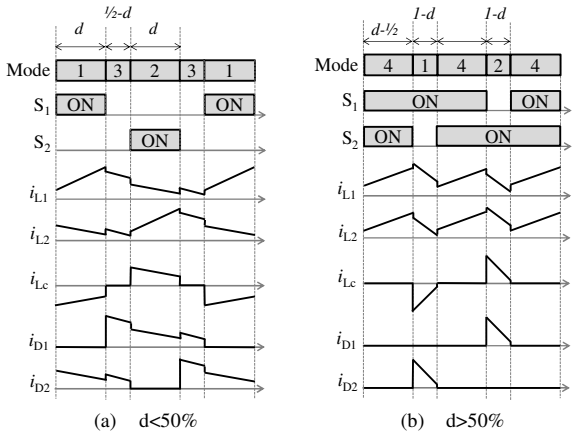

Fig. 6. Operating waveforms.

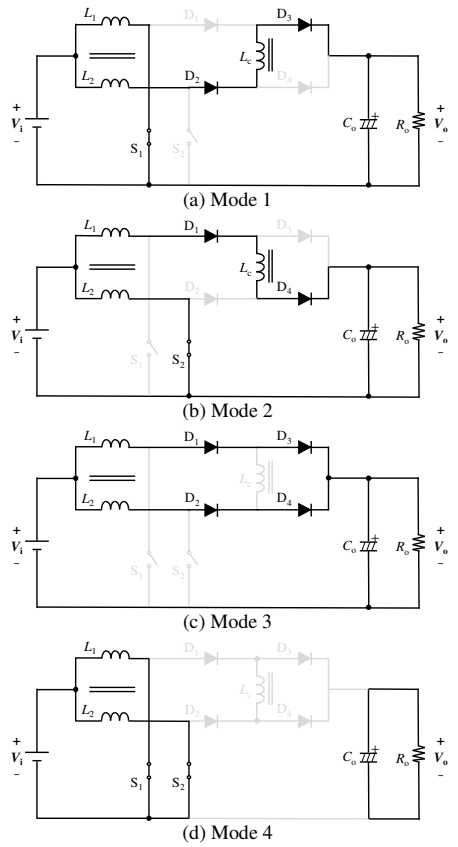

Fig. 7. Operation modes.

Consequently, based on the two loops of Fig. 7(a) it is possible to derive:

$$V_i = N_o \frac{\Delta\phi_1}{T_1} \quad (6)$$

$$V_i = N_o \frac{\Delta\phi_2}{T_1} - N_c \frac{\Delta\phi_c}{T_1} + V_o \quad (7)$$

Where $\Delta\phi_1$, $\Delta\phi_2$ and $\Delta\phi_c$ are the magnetic flux variations in the windings L_1, L_2 and L_c, respectively. And, T_1 is the time duration of Mode 1.

Mode 2: Based on Fig. 6 and Fig. 7(b), S_1 is turned OFF and S_2 is turned ON, i_1 flows through L_1, D_1, D_4, L_c and C_o. In contrast, i_2 flows only through the winding L_2. In addition, a positive voltage is induced in the central winding L_c and therefore the current flows through L_c rather than through D_2 and D_3.

Taking into account the operating principle of each loop in Mode 2, it is possible to derive:

$$V_i = N_o \frac{\Delta\phi_1}{T_2} + N_c \frac{\Delta\phi_c}{T_2} + V_o \tag{8}$$

$$V_i = N_o \frac{\Delta\phi_2}{T_2} \tag{9}$$

Where T_2 is defined as the time of Mode 2.

Mode 3: As Fig. 6 and Fig. 7(c) show, S_1 and S_2 are turned OFF and i_1 flows through L_1, D_1, D_3 and C_o; while i_2 flows through L_2, D_2, D_4 and C_o.

Based on Fig. 7(c) and the operation explained before, we can derive:

$$V_i = N_o \frac{\Delta\phi_1}{T_3} + V_o \tag{10}$$

$$V_i = N_o \frac{\Delta\phi_2}{T_3} + V_o \tag{11}$$

Where T_3 is the time duration of Mode 3.

Mode 4: Finally, as Fig. 6 and Fig. 7(d) show, S_1 and S_2 are turned ON, where i_1 flows only through L_1, and i_2 through L_2. All four diodes remain OFF and there is no current flowing through the central winding of the coupled inductor. Consequently, the loops expressions can be derived as:

$$V_i = N_o \frac{\Delta\phi_1}{T_4} \tag{12}$$

$$V_i = N_o \frac{\Delta\phi_2}{T_4} \tag{13}$$

Where T_4 is the duration of Mode 4.

B. Voltage Gain

According to the steady-state analysis presented before, it is possible to establish the relationship between each operating mode and the duty cycle. Therefore, the voltage gain M, defined as the ratio of the output and input voltage, in function of the duty cycle d when it is lower than 50% can be obtained from (6), (8) and (10).

This is possible by the equality to zero of $\Delta\phi_1$ or $\Delta\phi_2$ through one cycle of operation, where V_i and V_o are isolated to find the voltage gain. Conclusively, the voltage gain when the duty cycle is lower than 50% is derived as follows:

$$M_{D<0.5} = \frac{1+N}{(1+N)-d(1+2N)} \tag{14}$$

On the other hand, from (6), (8) and (12), the voltage gain when the duty cycle is higher than 50% is expressed as:

$$M_{D>0.5} = \frac{1+N}{1-d} \tag{15}$$

Compared to the converters proposed in [16]–[20], the proposed converter offers higher voltage gain at low duty cycle. Certainly, some converters, e.g. [19], offer a similar gain, but they have to use several multiplier cells that may increase the mass and volume of the entire converter.

IV. Magnetic Modeling

With the purpose of analyzing the current behavior of each winding in both coupled-inductor configurations ICI and TCCI, the magnetic modeling of each configuration is required.

In this case, for convenience in the calculation, a general magnetic circuit model generic for both configurations is introduced in Fig. 8. The reason why this model is applicable to both configurations is shown in the Appendix.

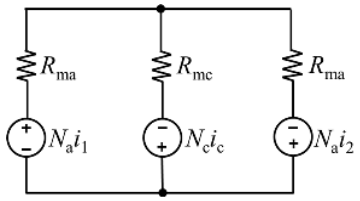

Fig. 8. General magnetic circuit model.

In this generic model, each magneto-motive force ($N \cdot i$) is applicable for both models because, as Fig. 2 to 5 and Eq. (2) show, windings L_1 and L_2 are directly coupled while the central winding L_c is crossed by both fluxes (ϕ_1 -ϕ_2).

On the other hand, the magnetic reluctances of this generic model are different in both inductor configurations. Therefore, the magnetic reluctances of the ICI configuration are defined as:

$$\begin{cases} R_{ma} = R_e \\ R_{mc} = R_c \end{cases} \tag{16}$$

Where R_e and R_c are defined as the reluctances of the externals and central leg, respectively, of the EE core of the ICI configuration, see Fig. 2 and 4.

While the magnetic reluctances of the TCCI configuration can be defined as:

$$\begin{cases} R_{ma} = R_c + \dfrac{R_e}{2} \\ R_{mc} = 0 \end{cases} \tag{17}$$

In this case, for convenience in the calculation, the reluctances of the TCCI configuration are defined in function of the independent core used for the ICI. The complete derivation of Eq. (16) and (17) is shown in the Appendix.

In this context, the generic model of Fig. 8 can be applied for the windings current calculation for both inductor configuration, having in mind that the magnetic reluctances are different as it was explained before. Consequently, on the base of the Faraday's law, the magnetic loops of Fig. 8 can be described as:

$$N_a i_1 + N_c i_c = R_{ma}\phi_1 + R_{mc}(\phi_1 - \phi_2) \quad (18)$$

$$N_a i_2 - N_c i_c = R_{ma}\phi_2 - R_{mc}(\phi_1 - \phi_2) \quad (19)$$

Consequently, based on the steady-state analysis and Fig. 7(a), the central winding current during Mode 1 is defined as:

$$I_c = -I_2 \quad (20)$$

Therefore, in Mode 1, substituting (20) into (18) and (19) yields:

$$I_1 = \frac{[N_a(R_{ma}+R_{mc})+N_c R_{ma}]\phi_1 + (N_c R_{ma} - N_a R_{mc})\phi_2}{N_a(N_a+N_c)} \quad (21)$$

$$I_2 = \frac{(R_{ma}+R_{mc})\phi_2 - R_{mc}\phi_1}{N_a+N_c} \quad (22)$$

Based on Fig. 7(b), the central winding current in Mode 2 is defined as:

$$I_c = I_1 \quad (23)$$

Consequently, from (23), (18) and (19) the current of L_1 and L_2 in Mode 2 is:

$$I_1 = \frac{(R_{ma}+R_{mc})\phi_1 - R_{mc}\phi_2}{N_a+N_c} \quad (24)$$

$$I_2 = \frac{[N_a(R_{ma}+R_{mc})+N_c R_{ma}]\phi_2 + (N_c R_{ma} - N_a R_{mc})\phi_1}{N_a(N_a+N_c)} \quad (25)$$

Then, taking into account the steady state analysis and Fig. 7(c), there is no current flowing through the central winding during Mode 3. Thereby, it is possible to derive:

$$I_1 = \frac{1}{N_a}[(R_{ma}+R_{mc})\phi_1 - R_{mc}\phi_2] \quad (26)$$

$$I_2 = \frac{1}{N_a}[(R_{ma}+R_{mc})\phi_2 - R_{mc}\phi_1] \quad (27)$$

Finally, as Fig. 7(d) shows, there is no presence of current flowing through the central winding during Mode 4 and therefore the current of L_1 and L_2 present the same value of Eq. (26) and (27), respectively.

Conclusively, and based on the windings current presented in each mode, it is possible to see that the current flowing through each winding has a different behavior dependent on the magnetic reluctance of each configuration.

Nonetheless, the total input current, i.e. I_1+I_2, is always equal to $R_{ma}/N_a \cdot (\phi_1+\phi_2)$, regardless to the operating modes. This indicates that the waveform of the total input current is continuous because fluxes ϕ_1 and ϕ_2 should be continuous according to Faraday's law. Therefore, the proposed converter can offer small input current ripple, although the waveform of each phase current can have significant discontinuity.

V. Experimental Validation

In order to verify the operating principle of the proposed converter, and to compare the effectiveness of each inductor configuration, three 100W prototypes were constructed and experimentally tested.

The experimental tests evaluate the voltage gain of the two types of coupled-inductor, shown in Fig. 2 to 5 and the input current of the proposed converter. Table I shows the experimental parameters of the ICI and TCCI prototypes and Fig. 9 shows the experimental setup of the ICI converter.

TABLE I
Experimental Parameters

		ICI	TCCI
Input Voltage	V_i	10.1V – 80.7V	12.5V – 82.4V
Output Voltage	V_o	100V	
Output Power	P_o	100W	
Frequency	f	30kHz	
Number of Turns	N	External: 16 turns Center: 32 turns	External: 16 turns Center: 32 turns
Inductance	L	L_1: 380 µH L_2: 378 µH L_c: 1.87 mH	L_1: 210 µH L_2: 231 µH L_c: 1.86 mH
Window area	A_w	642 mm^2	396 mm^2
Sectional area	A_{core}	280 mm^2	247 mm^2
Volume	V_e	40420 mm^3	27100 mm^3 each

These prototypes were constructed using SiC Diodes, CoolMos, Multilayer Capacitors and the mentioned coupled-inductors with a ratio of turns of $N=2$. In fact, the third prototype corresponds to the conventional interleaved two-phase boost converter which is constructed with the purpose of comparing the voltage gain of the proposed converter.

Fig. 10 shows the experimental results of the voltage gain of the proposed high step-up converter with the two configurations of coupled-inductors. This figure also shows the theoretical voltage gain at $N=2$. In addition, the experimental voltage gain of the conventional two-phase interleaved boost converter is presented as well.

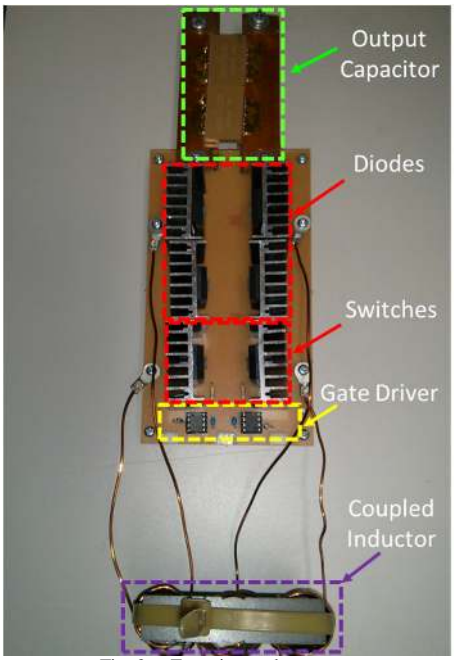

Fig. 9. Experimental setup.

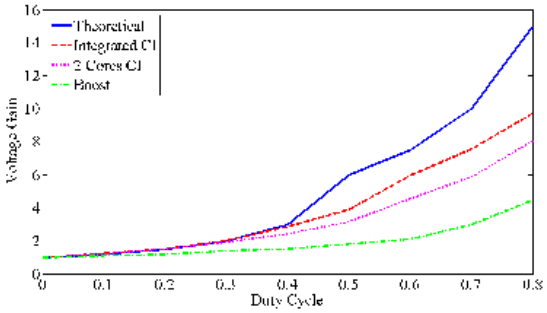

Fig. 10. Voltage gain vs. Duty cycle.

The results revealed that both prototypes of the proposed converter show a higher voltage gain compared to the conventional boost chopper, particularly in duty cycles higher than 0.5. In addition, the voltage gain of the integrated coupled-inductor was 20% higher than the two cores coupled-inductor when the converter is operating at a duty cycle of 80%.

However, the experimental results present lower voltage gain in comparison to the theoretical calculation; this may be caused by the parasitic resistance and the stray inductance in the coupled-inductor [25]. Consequently, the effectiveness of the integrated coupled inductor in the proposed converter is demonstrated.

Moreover, Fig. 11 shows the experimental waveforms of the gate-source voltage V_{GS1} and the winding current i_{L1} of the proposed high step-up converter with the integrated coupled-inductor as a validation of the operating waveforms illustrated in Fig. 6.

Based on Fig. 11, it is possible to affirm that the winding current i_{L1} and its dual i_{L2} have a discontinuous behavior. However, the integration of these two waveforms shapes a continuous input current, as shown in Fig. 12.

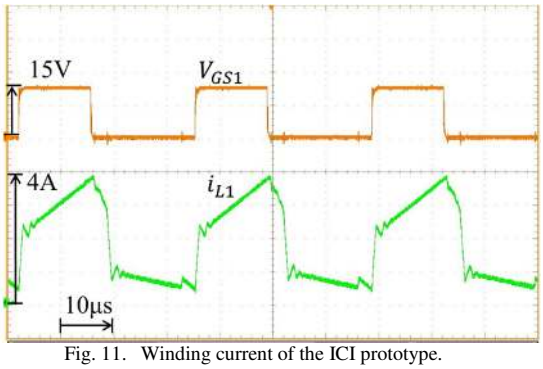

Fig. 11. Winding current of the ICI prototype.

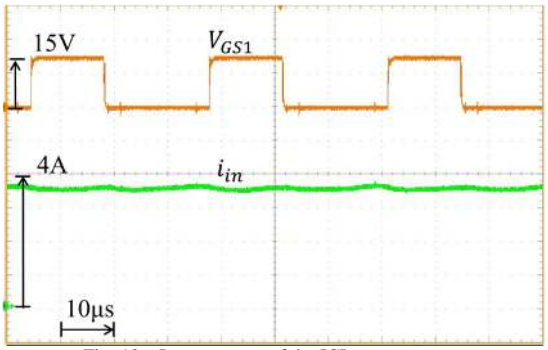

Fig. 12. Input current of the ICI prototype.

Finally, the input current ripple i_{in} of the proposed converter with ICI configuration was measured and compared with the input current ripple of the conventional interleaved two-phase boost converter. As a result, the proposed converter presents a normalized input current ripple of 8.33%, while the conventional topology has a ripple of 10%. Therefore, the effectiveness of the proposed converter is validated.

VI. Conclusion

This paper investigates a novel high step-up two-phase interleaved boost converter and its behavior with two different configurations of coupled-inductor. First, this paper analyzes the operating principle and the steady-state of the proposed converter. From this analysis, the voltage gain performance of the proposed converter was calculated and compared to other high step-up topologies proposed in the literature. Then, two coupled-inductors were presented and a performance comparison was conducted to evaluate the effectiveness of the integrated coupled-inductor in comparison to the two cores coupled-inductor. The integrated coupled-inductor was found to exhibit a voltage gain 20% higher than the two cores coupled-inductor when the converter is operating at a duty cycle of 80% and a ratio of turns of 2. In addition, the proposed converter offers a reduction of the input current ripple in comparison to the conventional interleaved boost converter.

Consequently, taking into account the advantages of the proposed converter in terms of voltage gain, power density and input current ripple, the proposed converter can be a promising topology for sustainable energy systems and vehicular applications when a high voltage

gain and high power density is needed.

APPENDIX

This section introduces the deriving process of the equations (16) and (17). These equations can be derived on the basis of the magnetic modeling of each inductor configuration. In fact, this modeling procedure was conducted with the purpose of representing both configurations with only one model.

Fig A.1 shows the magnetic model of the ICI configuration.

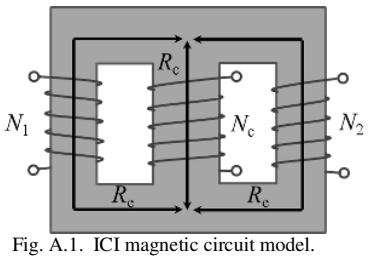

Fig. A.1. ICI magnetic circuit model.

From this model, it is possible to infer that each variable described in Fig. 8 corresponds to the same of Fig. A.1, as follows:

$$R_{ma} = R_e \tag{A1}$$

$$R_{mc} = R_c \tag{A2}$$

On the other hand, the modeling of the TCCI is more complicated. Fig. A.2 shows the reluctances in each core.

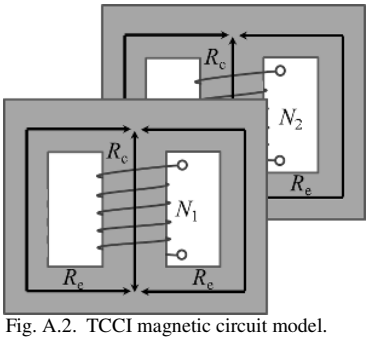

Fig. A.2. TCCI magnetic circuit model.

In addition, Fig A.3 shows the equivalent magnetic circuits of each independent core.

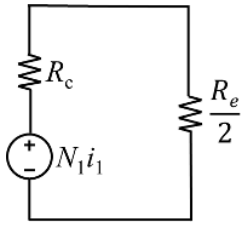

Fig. A.3. Equivalent circuit of each independent core in the TCCI configuration.

As Fig. A.3 shows, the equivalent circuit of each independent core of the TCCI configuration is simplified by the parallel of both reluctances of the external legs ($R_e/2$) plus the reluctance of the central leg R_c.

Therefore, the magnetic circuit of each independent core of the TCCI can be described as:

$$N_1 i_1 + N_c i_c = \left(R_c + \frac{R_e}{2} \right) \phi_1 \tag{A3}$$

$$N_2 i_2 - N_c i_c = \left(R_c + \frac{R_e}{2} \right) \phi_2 \tag{A4}$$

On the other hand, for the derivation of the reluctance of the center of both cores, where there are both central legs and air, it is necessary to consider the base of Faraday's law and Ampere's law. Therefore, in order to satisfy Eq. (A3) and (A4), it is possible to infer that the value of R_{mc}, in the generic model for the case of the TCCI, has to be zero.

Finally, as a conclusion, the reluctances of the TCCI can be defined as:

$$R_{ma} = R_c + \frac{R_e}{2} \tag{A5}$$

$$R_{mc} = 0 \tag{A6}$$

REFERENCES

[1] B. Yang, W. Li, Y. Zhao, and X. He, "Design and Analysis of a Grid-Connected Photovoltaic Power System," *IEEE Trans. Power. Electron*., vol. 4, no. 25, pp. 992-1000, 2010.

[2] R.J. Wai, C.Y. Lin, R.Y. Duan, and Y.R. Chang, "High Efficiency DC-DC Converter With High Voltage Gain and Reduced Switch Stress," *IEEE Trans. Ind. Electron*., vol. 54, no. 1, pp. 354-364. 2007.

[3] W. Li, J. Liu, J. Wu and X. He, "Design and Analysis of Isolated ZVT Boost Converters for High-Efficiency and High-Step-Up Applications," *IEEE Transactions on Power Electronics*, vol. 22, no. 6, pp. 2363-2374, 2007.

[4] K. Park, G. Moon and M. Youn, "Nonisolated High Step-Up Stacked Converter Based on Boost-Integrated Isolated Converter," *IEEE Transactions on Power Electronics*, vol. 26, no. 2, pp.577-587. 2011.

[5] W. Li, and X. He, "ZVT interleaved boost converters for high-efficiency, high step-up DC-DC conversion," *IEEE Transactions on Power Electronics,* vol. 1, no. 2, pp. 284-290, 2007.

[6] W. Rong and D. Rou, "High Step-Up Converter with Coupled-Inductor," *IEEE Trans. Power Electron.,* vol. 20, no. 5, pp. 1025-1035, 2005.

[7] W. Rong and D. Rou, "High Step-Up Coupled-Inductor-Based Converter Using Bi-direction Energy Transmission," *IEEE Power Electronics Specialists Conference PESC,* pp. 406-412, 2005.

[8] R. Gules, L. Pfitscher and L. Franco, "An Interleaved Boost DC-DC Converter with Large Conversion Ratio," *IEEE International Symposium on Industrial Electronics, ISIE*, pp. 411-416, 2003.

[9] K. Hwu, W. Tu and C. Lin, "Two Types of High Step-Up DC-DC Converters Based on Charge Pump and Coupling Inductor," *International Review of Electrical Engineering,* vol. 6, no. 3, pp. 1130-1139, 2011.

[10] K. Hwu, Y. Yau and J. Shieh, "High Step-Up Converter Based on Coupling Inductor and Bootstrap Capacitors With Active Clamping," *IEEE Third International Conference on Sustainable Energy Technologies (ICSET)*, pp.364-368, 2012.

[11] W. Martinez, M. Yamamoto, P. Grbovic and C. Cortes, "Efficiency Optimization of a Single-Phase Boost DC-DC Converter for Electric Vehicle Applications," *IEEE 40th Annual Conference of the IEEE Industrial Electronics Society – IECON*, pp. 1-6, 2014.

[12] K. Tseng and J. Lin, "High step-up DC/DC converter for fuel cell hybrid electric vehicles," *2013 IEEE International Symposium on Next-Generation Electronics (ISNE),* pp. 498-501. 2013.

[13] W. Martinez, C. Cortes and L. Munoz, "Sizing of Ultracapacitors and Batteries for a High Performance Electric Vehicle," *IEEE International Electric Vehicle Conference – IEVC*, pp. 535-541, 2012.

[14] M. Pavlovsky, G. Guidi and A. Kawamura, "Assessment of Coupled and Independent Phase Designs of Interleaved Multiphase Buck/Boost DC–DC Converter for EV Power Train," *IEEE Transactions on Power Electronics*, vol.29, no. 6, pp.2693-2704. 2014.

[15] S. Kimura, J. Imaoka and M. Yamamoto, "Downsizing effects of integrated magnetic components in high power density DC-DC converters for EV and HEV," *IEEE Energy Conversion Congress and Exposition (ECCE)*, pp. 5761 – 5768, 2014.

[16] K. Park, G. Moon and M. Youn, "Nonisolated High Step-Up Stacked Converter Based on Boost-Integrated Isolated Converter," *IEEE Transactions on Power Electronics*, vol. 26, no.2, pp.577-587. 2011.

[17] W. Li, X. Xiang, C. Li, W. Li and X. He, "Interleaved High Step-Up ZVT Converter with Built-In Transformer Voltage Doubler Cell for Distributed PV Generation System," *IEEE Transactions on Power Electronics*, vol. 28, no. 1, pp. 300-313. 2013.

[18] K. Hwu and Y. Yau, "High Step-Up Converter Based on Coupling Inductor and Bootstrap Capacitors With Active Clamping," *IEEE Transactions on Power Electronics*, vol.29, no. 6, pp.2655,2660, 2014.

[19] S. Dwari and L. Parsa, "An Efficient High-Step-Up Interleaved DC–DC Converter With a Common Active Clamp," *IEEE Transactions on Power Electronics*, vol.26, no. 1, pp. 66-78, 2011.

[20] W. Li, W. Li and X. He, "Zero-voltage transition interleaved high step-up converter with built-in transformer," *IEEE Transactions on Power Electronics,* vol. 4, no. 5, pp.523-531, 2011.

[21] M. Hirakawa, M. Nagano, Y. Watanabe, K. Andoh, S. Nakatomi and S. Hashino, "High Power Density DC/DC Converter using the Close-Coupled Inductors," *1st IEEE Energy Conversion Congress and Exposition (ECCE),* pp.1760-1767. 2009.

[22] J. Imaoka, S. Kimura, W. Martinez and M. Yamamoto, "A Novel Integrated Magnetic Core Structure Suitable for Transformer-linked Interleaved Boost chopper Circuit," *IEEJ Journal of Industry Applications*, vol.3, no.5, pp. 395-404, 2014.

[23] W. Martinez, S. Kimura, J. Imaoka, M. Yamamoto, K. Umetani, S. Arimura and T. Hirano, "High Power Density DC-DC Converter for Home Energy Management Systems," *International Conference on Intelligent Green Building and Smart Grid – IGBSG,* pp, 1-6, 2014.

[24] A. Nishigaki, W. Martinez, H. Umegami, F. Hattori and M. Yamamoto, "An Analysis of False Turn-On Mechanism on Power Devices," *IEEE Energy Conversion Congress and Exposition- ECCE*, pp. 2988-2993, 2014.

[25] W. Martinez, J. Imaoka, M. Yamamoto and K. Umetani, "Parasitic Resistance Analysis in a Novel High Step-Up Interleaved Converter for Hybrid Electric Vehicles," *Journal of the Japan Institute of Power Electronics*, vol. 40, no. 1, pp. 93-104, 2015.